Materials Research Bulletin 181 (2025) 113076

Contents lists available at ScienceDirect

Materials Research Bulletin

journal homepage: www.elsevier.com/locate/matresbu

Research Papers

A humidity tolerance and room temperature carbon soot@ZIF-71 sensor for toluene vapour detection

Lesego Malepe [a], Tantoh Derek Ndinteh [a], Patrick Ndungu [b,*], Messai Adenew Mamo [a,*]

[a] Department of Chemical Sciences, University of Johannesburg, PO Box 17011, Doornfontein, 2028 Johannesburg, South Africa
[b] Department of Chemistry, University of Pretoria, Private Bag X20, Hatfield, 0028, Pretoria, South Africa

ARTICLE INFO

Keywords:
Sensitivity
Toluene
ZIF-71
Gas sensors
Room temperature

ABSTRACT

The Solid-state chemiresistive gas sensing devices are the desirable recruit to detect toxic gases and volatile organic compounds; however, the growth of real-life applications of these sensors is poor due to their drawbacks, including high working temperature, showing poor responses during moderate to high humidity, and poor selectivity towards the gas of interest. In this work, we synthesised zeolitic imidazolate framework (ZIF-71), carbon soot (CNPs) and CNPs@ZIF-71 composite and were successfully characterised using scanning electron microscopy (SEM), transmission electron microscopy (TEM), powder X-ray diffraction (PXRD), Raman spectroscopy, Fourier-transform infrared spectroscopy (FTIR), and X-ray photoelectron spectroscopy (XPS). The ZIF-71, CNPs and CNPs@ZIF-71 composites are used to fabricate the sensors to detect toluene, ethanol, mesitylene, diethyl ether and acetonitrile vapours at room temperature. The ZIF-71 did not respond to any of the tested VOCs at room temperature; however, the CNPs sensor showed some little response to the tested VOCs. However, the linear response was not observed as the analyte concentration increased. However, the CNPs@ZIF-71 showed excellent response and sensitivity towards the toluene vapour and less sensitivity towards mesitylene, diethyl ether, acetonitrile and ethanol vapours. ZIF-71 synergistically improves CNPs sensing performances on toluene vapour detection. The CNPs@ZIF-71 sensor was found to be highly resistive during the detection of toluene vapour. The calculated limit for the detection of toluene vapour on the CNPs@ZIF-71 composite sensor was 518 ppb. In situ, FTIR coupled with LCR meter online analysis was done to study the sensing mechanism, and it was found that toluene vapour detection on sensor 3 undergoes total deep oxidation to form H_2O and CO_2 as by-products.

1. Introduction

There is **a** worldwide growth of environmental air pollution due to industrialisation, mainly in the chemical and mining industries. These industries use toxic chemicals daily end in releasing various toxic vapours into the atmosphere. Consumer goods have increased significantly due to an exponential increase in the global population [1,2]. Some companies release volatile organic compounds (VOCs) while producing food, electricity, and other basic needs. The VOCs may include benzene, toluene, acetone, mesitylene, methanol, carbon monoxide, ammonia, hydrogen sulfide, nitrogen dioxide and many more. Toluene is an organic compound that effortlessly evaporates at room temperature because of its high vapour pressure. Toluene liquids are commonly used as solvents in petrochemical, agricultural processes, and other industrial applications, including adhesives, inks, pharmaceuticals, and laboratories [3,4]. A severe inhalation of toluene vapour may result in human dizziness, drowsiness, and respiratory tract irritation [5]. Human inhalation of toluene vapour has a threshold for eye and nose irritation as low as 53.07 ppm, and as low as 265.37 ppm, which can make a person dizzy [6]. In the past, the accurate detection of gases and VOCs involved using analytical instruments such as gas chromatography [7], optoacoustic [8], and spectrophotometer [9], unfortunately, these analytical instruments possess some drawbacks that lead them not being widely available due to their expensiveness, requiring high maintenance, trained personnel, not portable, and long time for analysis. Over the years, semiconductor metal oxide (SMO) chemo-resistive gas sensors gained a lot of attention from researchers and engineers to deploy them to detect harmful gases and VOCs due to their low cost in fabrication, portability, high sensitivity, high response-recovery time and fast analysis time [10]. Basically, chemiresistive gas sensors are the sensors that

* Corresponding authors.
E-mail addresses: patrick.ndungu@up.ac.za (P. Ndungu), messaim@uj.ac.za (M.A. Mamo).

https://doi.org/10.1016/j.materresbull.2024.113076
Received 15 April 2024; Received in revised form 4 July 2024; Accepted 2 September 2024
Available online 5 September 2024

measure a change in electrical resistance once the material (previously SMOs) used to fabricate the sensor interacts with gases or volatile organic compounds [11]. Chemiresistive gas sensors are built by making a thin film of sensing materials on the interdigitated gold electrodes. Electrodes are commonly plated with gold (Au) or platinum (Pt) because of their excellent conductivity and corrosive resistivity. However, the previously reported SMOs gas sensors lack selectivity towards the aimed gas to detect in the presence of other gases [12], possess poor gas response in high humidity conditions, and operate at extremely high temperatures of 240–400 °C [10,13]. It is not ideal to use high-temperature working sensors because of their high energy consumption, which is unsuitable for the energy economy.

Interestingly, carbon materials such as carbon fibres [14], carbon nanoparticles [15], graphene oxide [16] and carbon nanotubes [17] are commonly used to allow the sensors to work at room temperatures. The significance of this work is to fill the gap posed by the previously reported materials, wherein the limitations include failure to maintain similar sensing responses as the humidity changes, poor selectivity towards a gas of interest, high working temperatures [10,13,18] and also a lack of proving the sensing mechanism. To address the poor response at high humidity levels and selectivity on the targeted gases or VOCs possessed by SMO and carbon-based gas sensors. Zeolitic imidazolate frameworks (ZIFs) are used as sensing material to allow the sensor to resist humidity during gas detection. ZIFs are promising materials to be deployed in gas sensing applications because of their easy synthesis, hydrophobic nature, and porosity tunability [11]. ZIFs are a subset of metal-organic frameworks (MOFs) composed of a central metal ion and imidazole linker [19–21]. A rarely reported material, ZIF-71, is made up of 4,5-dichloroimidazole and a Zn^{2+} possessing tetrahedral geometry. However, deploying ZIFs only as sensing materials in gas sensors still possesses a disadvantage: not operating at room temperature but at elevated temperatures 140 to 350 °C [19,20]. Recently, using carbon soot (commonly known as carbon nanoparticles [CNPs]) hybridised with other materials become a focused area of research due to their ability to work at room temperature and fast response-recovery times. The CNPs are inexpensive and easy to prepare. In this work, we use ZIF-71, CNPs, and ZIF-71@CNPs composite as sensing material to detect VOCs at room temperature. Furthermore, the mass of CNPs in CNPs@ZIF-71 composite sensors was varied, while the mass of ZIF-71 was kept constant to investigate the sensitivity of the VOCs.

2. Experimental

2.1. Chemicals and reagents

Zinc acetate dihydrate [$Zn(CH_3COO)_2{\cdot}2H_2O$], 4,5-dichlorolimidazole [dclm] (99%), N, N-dimethylformamide (DMF, 99.5%), ethanol [EtOH], mesitylene (commonly known as 1,3,5—trimethylbenzene), acetonitrile, diethyl ether, (98%), and toluene (C_7H_8, 99.8%), were purchased from Sigma Aldrich (South Africa). Lighthouse candles were purchased at a local supermarket in Johannesburg, South Africa.

2.2. Synthetic methods

2.2.1. preparation of carbon nanoparticles (CNPs)

The pyrolysis method is the method opted to prepare CNPs, as reported by the referenced work [15]. A ceramic cup was placed about 2 cm above the flame of the burning candle that produces smoke for the collection of CNPs. The ceramic cup with the CNPs was cooled at room temperature, and a spatula was used to scrape the accumulated CNPs from the ceramic cup's internal walls. The scraped CNPs were washed with ethanol three times and dried in the oven at 60 °C for 12 h. The washed CNPs were stored in a vial at room temperature until used.

2.2.2. Synthesis of ZIF-71 and CNPs@ZIF-71

The synthesis of ZIF-71. Firstly, 110 mg $Zn(CH_3COO)_2).2H_2O$ and 160 mg of dclm were separately dissolved in 5 mL DMF and 5 mL methanol, respectively. The two solutions were stirred until the homogeneous mixtures were obtained and then the zinc-containing solution was transferred into the dclm linker solution to form ZIF-71. The ZIF-71 **solution** was stirred for 30 min, and after the reaction completion, the ZIF-71 was extracted by centrifuging the solution for 1 hour. The pink product was dried using an oven at 60 °C for 12 h [22]. A mechanical mixing method was used to prepare CNPs@ZIF-71 composite, wherein a 1:1 mass ratio of CNPs and ZIF-71 were dissolved in DMF. The black solution was dissolved and stirred at room temperature for 18 h. After the time elapsed, the solution was dried at 80 °C for 24 h [23].

2.2.3. Sensor fabrication

CNPs, ZIF-71 and CNPs@ZIF-71 are the sensing materials utilised in fabricating the sensors to detect VOCs at room temperature. 10 mg ZIF-71 and 10 mg CNPs were singlely dissolved in 5 mL DMF to prepare sensors 1 and 2. To prepare sensor 3, 10 mg ZIF-71 and 10 mg CNPs were both dissolved in a 5 mL DMF contained in a glass vial and to prepare sensor 4 and sensor 5, the mass of CNPs were varied within the composite while the mass of CNPs were kept constant (see Table 1). All the mixtures were ultrasonicated and stirred at room temperature for 12 h to obtain a homogeneous mixture. 7μL of mixtures of each composite were taken from and drop coated on a gold plated-interdigitated electrode to prepare the sensors and allowed to dry at room temperature. All the prepared sensors were placed in a vacuum desiccator for three days to dry the DMF, following a similar reported work [24].

2.2.4. gas sensing set-up

The same set-up (Fig. 1) was used to investigate all prepared solid-state gas sensors. An E4980A keysight LCR meter was connected to the prepared gas sensor, which was then put inside a 20 L round bottom flask with four inlets. The two inlets of the round-bottom flask were connected to a vacuum pump, and the other introduced ambient air while any gas was being removed. The third inlet was to introduce the sensing device and the final one was for the relative humidity sensor. At a contact time of 10 min per injection, a total of five trials, 1, 2, 3, 4, and 5 μL of volatile organic compounds, were introduced into the round-bottom flask. Each trial was followed by a 3-minute rest period before the next one, during which the exposed vapour was flushed out with the help of a vacuum pump at atmospheric pressure. The analyte liquid has a high vapour pressure, which causes the volatile organic compounds (VOCs) to evaporate quickly during injection. We computed the vapour concentration of the volatile organic compounds (VOCs) using Eq. (1):

$$C = \frac{22.4\, p T V_s}{273\, M_r V} \times 1000, \quad (1)$$

Where C is the vapour concentration (ppm), p is the density of the liquid analyte ($g.cm^{-1}$), T is the temperature (K), V_s is the volume injected into the 20 L volumetric flask (μL), M_r is the molar mass of the liquid analyte and V is the volume of the volumetric flask (L) [15].

2.2.5. sensor's response and recovery tests

The gas sensor's response time was defined as the time needed for the sensor to reach 90% maximum response before it reaches the saturated (plateau) state, while recovery time was defined as 90% time required for the sensor to get its baseline during the removal of the gas exposed

Table 1
The prepared sensors and their respective mass ratios.

Sensor name	Sensing material	Mass (mg), CNPs:ZIF-71
Sensor 1	ZIF-71	0:10
Sensor 2	CNPs	10:0
Sensor 3	CNPs@ZIF-71	10:10
Sensor 4	CNPs@ZIF-71	20:10
Sensor 5	CNPs@ZIF-71	30:10

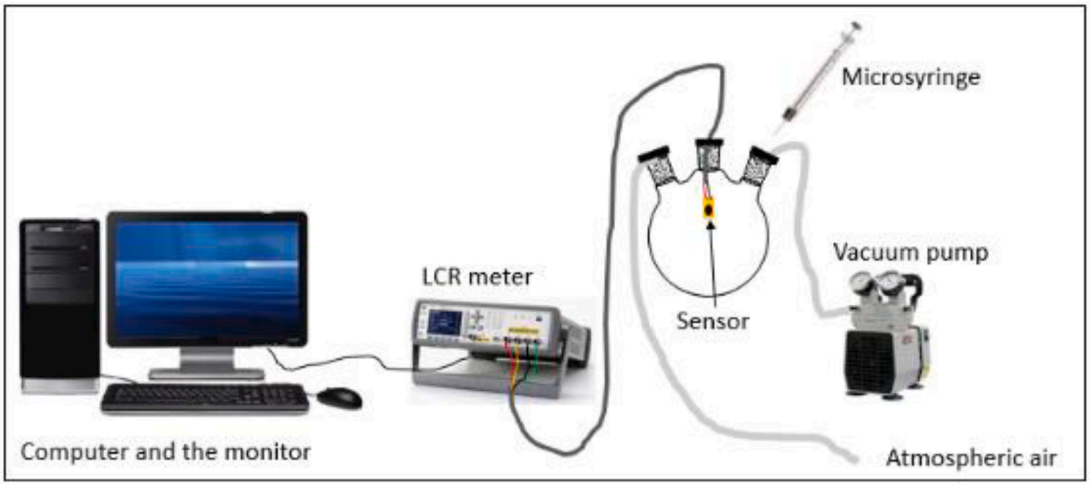

Fig. 1. Gas sensing set-up.

from its plateau.

2.2.6. An in situ FTIR-online LCR meter measurement

The *in-situ* FTIR -LCR meter set-up was followed as reported [24]. IR spectra were recorded using the FTIR instrument (PerkinElmer Spectrum 100) with a resolution of 4 cm^{-1} and 16 scans. A gas cell is a cylindrical cell (approximately 110 mL volume) fitted with two KBr windows at both ends. The vessel with two inlets for the sample injection and the sensors' electrical connection was placed at the centre, with the device positioned on the upper wall of the cell so that the IR beam passes through the windows without blocking. The sensor was connected to the LCR meter through two electrically insulated wires. During the measurement, the sensor was exposed to about 382 ppm of the analyte vapour and the vessel was kept closed throughout the experiment. FTIR spectra were taken every 1 min, while the impedance measurements were taken continuously for each sensor to a total maximum time of 22 min.

2.2.7. Humidity tests

Relative Humidity (RH) tests were done at room temperature (23 °C), wherein a humidity sensor and the gas sensor were both placed inside the sensing chamber. The chamber's humidity was varied by carefully controlling the volume of water vapour from boiling water into the chamber. Thus, the sensor detected toulene vapour at various relative humidity conditions [24].

2.2.8. Characterisation techniques

The morphology of ZIF-**71**, CNPs and CNPs**@**ZIF-**71** were investigated using high-resolution transmission electron microscopy (HRTEM) at an acceleration voltage of 200 kV, JEOL-TEM 2010 (Japan) using Gatan software wherein samples were loaded onto copper grids. Powder X-ray diffraction (PXRD) was done using a Bruker D2 Phaser using LynxEye detector with radiation of a CuKα at a wavelength of 0.154 nm. A Bruker Senterra laser Raman spectrometer fitted with a frequency-doubled Nd-YAG laser with a wavelength of 532 nm was used for Raman analysis. Fourier transform infrared spectroscopy (FTIR, Bruker-Alpha, Germany) was used to identify chemical functionalities on the materials.

3. Results and discussion

3.1. Materials characterisations

The surface morphology of the synthesised materials was investigated using SEM. The CNPs are found to be perfectly rounded particles and the spherical particles are bound to each other to form large irregular structures (see Fig. 2**a**). The SEM image reveals that the ZIF-71 are well-perfected hexagonal shapes of different diameter sizes ranging between 120 - 350 nm (see Fig. 2**c**). The SEM image of the CNPs@ZIF-71 composite as shown in Fig. 2**e**, wherein it revealed that the carbon nanoparticles covered the surface of hexagonal ZIF-71. The CNPs@ZIF-71 has resulted in a rough surface due to agglomerated CNPs (see Fig. 2**e**). The SEM-EDX was also conducted to investigate the elements in the samples. The SEM-EDX displayed in Fig. 2**b** showed CNPs are composed of carbon (C) and oxygen (O) only, ZIF-71 and CNPs@ZIF-71 are composed of zinc (Zn), carbon (C), chlorine (Cl), and oxygen (O). Nitrogen from the imidazole ring is omitted because it does not have a K-shell level, and the EDX detects elements with K-shell levels (see Fig. 2**d and f**). Furthermore, the HR-TEM analysis was carried out to study the internal morphology of CNPs, ZIF-71, and CNPs@ZIF-71. The spherical CNPs appeared to be stacked on top of each other, forming chain-like structures (see Fig. 3**a and b**); the average diameter of the CNPs is 35 nm (see Fig. 3**e**). The **TEM** image**s** agree well with SEM images that the structures of ZIF-71 are hexagonal (see Fig. 3**c**). Fig. 3**d** clearly shows that the carbon nanoparticles are fused on the surface of the hexagonal ZIFs, **similar findings were reported** [25,26].

The phase purity and crystallinity analysis of CNPs, ZIF-71, and CNPs@ZIF-71 were investigated using powder X-ray diffraction (PXRD). The CNPs exhibit two broad peaks assigned for amorphous nature ($2\theta = 24.5°$) and graphitic character ($2\theta = 43.7°$), as shown in Fig. 4**a** [23]. The XRD pattern of ZIF-71, as displayed in Fig. 4**b**, matches the earlier report [27]. The XRD peaks positioned at $2\theta = 4.4°$, 6.2°, and $2\theta = 7.6°$, which are assigned for (001), (002), and (112) crystal planes, indicate a successful synthesis of ZIF-71 [28]. Due to the high crystallinity of ZIF-71, the two broad peaks of amorphous CNPs in CNPs@ZIF-71 XRD patterns are suppressed.

The chemical bonding and functional group analysis of CNPs, ZIF-71, and CNPs@ZIF-71 were studied using FTIR. The broad peak occurring at 3555 cm^{-1} on the CNPs FTIR spectrum is assigned for O—H stretching [25]. The two peaks occurring at 3232 cm^{-1} and 2906 cm^{-1} represent C—H stretchings. In addition, peaks positioned at 1645 cm^{-1}, 1388 $cm^{-1,}$ and 1105 cm^{-1} are for H—O-H and C = O stretching, C—OH stretching, and C—O bend stretchings (see Fig. 5) [22]. The ZIF-71 FTIR peaks at 2917 cm^{-1}, 1517 cm^{-1}, and 540^{-1} are assigned for C—H, C = N, and Zn-N, respectively [28,29]. The IR bands between 1193 and 1226 cm^{-1} are ascribed to the presence of 4,5-dichloroimidazole ligand [28]. The peaks on CNPs are also in the ZIF-71, thus, it is challenging to outline a few peaks to prove the formation of CNPs and ZIF-71 composite (see Fig. 5).

Figs. 6 and 7 show XPS spectra plotted for CNPs, ZIF-71, and

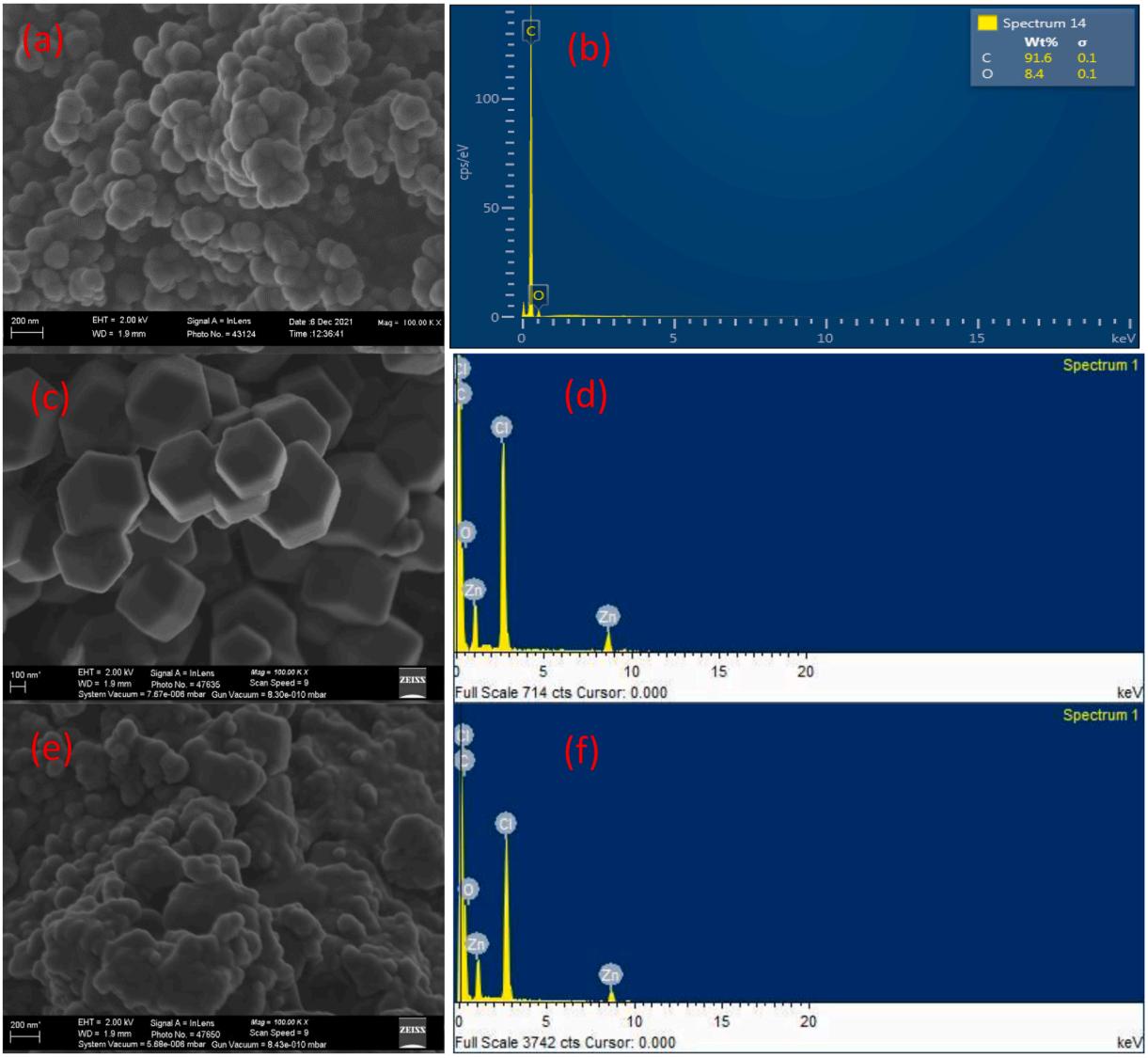

Fig. 2. SEM image of (a) CNPS, (b) ZIF-71, (c) CNPs@ZIF-71, and EDX spectra of (d) CNPs, (e) ZIF-71, and (f) CNPs@ZIF-71.

CNPs@ZIF-71 to reveal the oxidation of zinc, elemental composition, and the type of oxidation species present within the synthesised materials. The XPS survey spectrum of CNPs revealed the presence of C 1 s and O 1 s peaks assigned for carbon (C) and oxygen (O). The XPS survey spectrum of ZIF-71 and CNPs@ZIF-71 showed Cl 2p, C 1 s, N 1 s, O 1 s, and Zn 2p, proving the presence of chlorine (Cl), carbon (C), nitrogen (N), oxygen (O) and zinc (Zn), respectively (see Fig. 6**a–c**). Fig. 7**a** presents two pronounced peaks at 1045.6 eV and 1022.6 eV due to Zn $2p_{1/2}$ and Zn $2p_{2/3}$, respectively. The separated binding energy between Zn $2p_{1/2}$ and Zn $2p_{2/3}$ is 23 eV [30], indicating the existence of Zn^{2+} in both ZIF-71 and CNPs@ZIF-71. The C 1 s scan of CNPs is deconvoluted into peaks at 283.8 eV, 284.6 eV, 286 eV, 287.8 eV, 288.8 eV assigned for C—C sp^2, C—C sp^3, hydroxyl group (C—O), carbonyl group (C = O), and carboxyl group (O—C = O), respectively [31] (see Fig. 5**b**). XPS analysis agrees well with XRD analysis (refer to Fig. 4) by proving the existence of the graphitic nature of the CNPs by showing a sp^2 hybridised peak on XPS. The fitted sp^2 and sp^3 XPS peaks were used to calculate their ratio, wherein the sp^2/sp^3 ratio was found to be 1.65. Using a ratio value of 2 as a reference, and since our sp^2/sp^3 ratio is less than 2, the CNPs are highly amorphous [31,32]. The C 1 s scan is fitted with two peaks at 284.6 eV and 286.6 eV for C = C and C = N/C—N from the imidazole ring of the ZIF-71 (see Fig. 5**c**). The XPS O 1 s spectra of CNPs, ZIF-71, and CNPs@ZIF-71 are fitted with peaks at 531.9 eV, and 533.2 eV assigned for O_β and O_γ, respectively. The beta oxygen (O_β) represents the oxygen species adsorbed on the surface of the materials, while the gamma oxygen (O_γ) represents the OH species adsorbed on the surface of the materials [32] (see Fig. 7**d–f**).

The O 1 s graphs are deconvoluted into oxygen species named O_β and O_γ. The curves are fitted with Gaussian to obtain the area under the curve for CNPs, ZIF-71 and CNPs@ZIF-71 composite with the mass ratio 1:1; the areas obtained were expressed in percentages as summarised in Table 2. All the tested sensing materials had both oxygen species, O_β and O_γ. The O_β content in CNPs@ZIF-71 composite improved from 18.8% to 50% with the material composition, and the higher amounts in O_β content play a crucial role in sensing.

3.2. *Gas sensing performances*

3.2.1. *Sensing performance, sensitivity, and response-recovery times*

The change in relative electrical resistances was recorded during the chemisorption interaction between the surface of the sensing materials (i.e. sensor 1 is composed of ZIF-71 only, sensor 2 is made up of CNPs, sensor 3 is made up of CNPs@ZIF-71 with the mass ratio 1:1, sensor 4 is made up of CNPs@ZIF-71 with the mass ratio 1:2, and sensor 5 is made

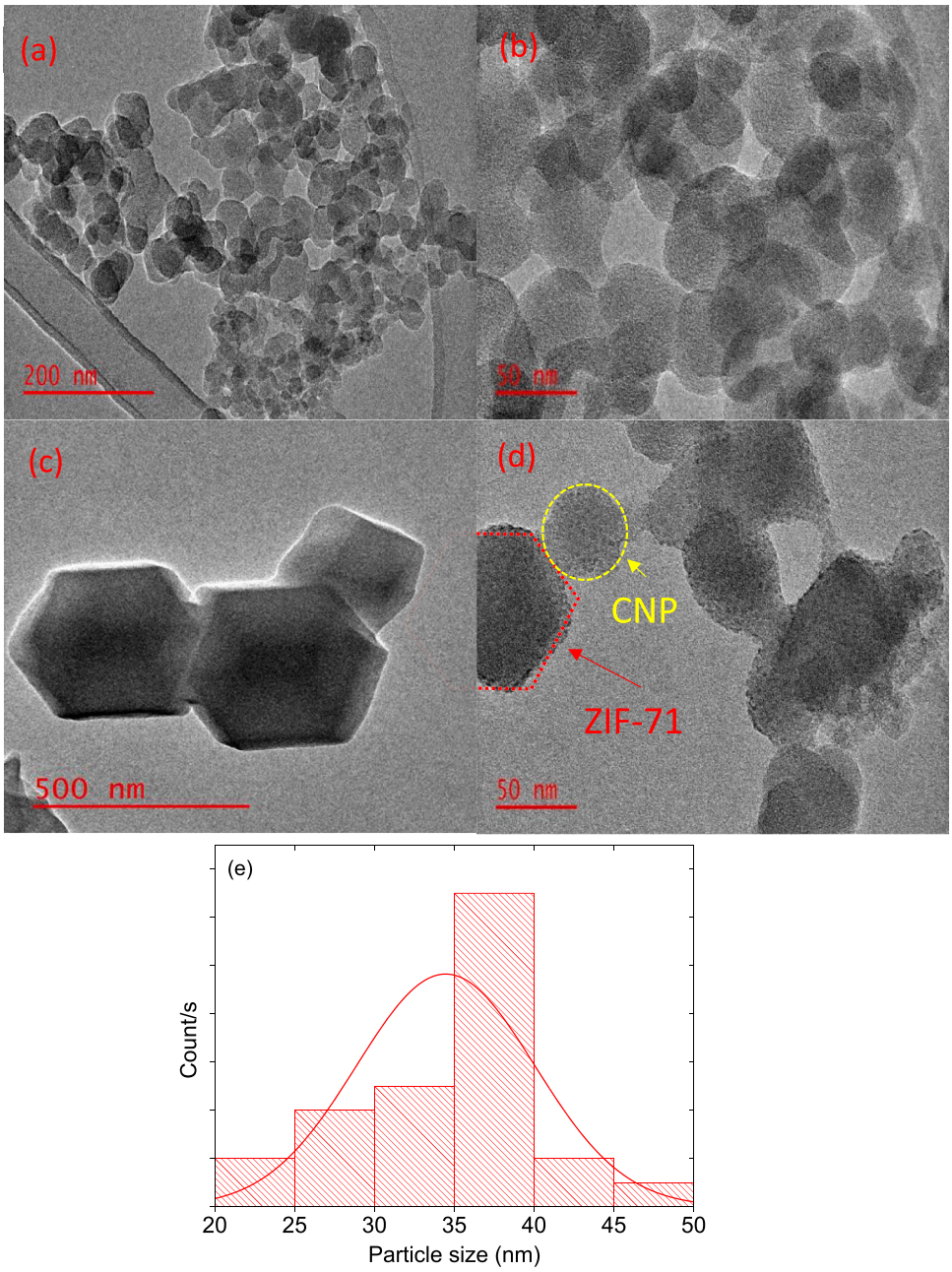

Fig. 3. TEM image of (a, b) CNPs, (c) ZIF-71, (d) CNPs@ZIF-71, and (e) particle size distribution of CNPs.

up of CNPs@ZIF-71 with the mass ratio 1:3) and the analytes (i.e. ethanol, toluene, mesitylene, diethyl ether and acetonitrile). The gas sensors' performances were tested at room temperature with an average relative humidity of 44%. Sensor 1 (ZIF-71) did not respond to any of the analytes at room temperature [19,20], while sensor 2 (CNPs) showed some interactions with the analytes; the recorded change in relative resistance is small (see **Fig. S.1**). The sensitivity of the sensors towards the analytes was improved when the ZIF-**71** was combined with the CNPs in sensors 3, 4, and 5. Since ZIF-71 did not respond to any analyte at room temperature, its mass within the CNPs@ZIF-71 composite was kept constant and the mass of CNPs varied to investigate the best sensor that possesses a good sensitivity and selectivity. The sensitivity of the sensors towards the detection of the analytes was calculated using the formula, i.e.

$$S = \frac{\Delta R}{\Delta C} \tag{2}$$

where S represents the sensitivity measured in Ωppm^{-1}, ΔR represents the change in relative resistance measured in ohms, and ΔC represents the change in concentration of the analyte in ppm [23]. The sensitivity of the sensors were recorded, while the mass of the CNPs within the CNPs@ZIF-71 composite changed.

Sensor 3 responded to all tested analytes, and it was found to be highly sensitive towards toluene vapour and less sensitive to diethyl ether, ethanol, mesitylene, and acetonitrile vapours. The sensor is approximately 45% more sensitive towards toluene (0.00625 Ωppm^{-1}) than the mesitylene (0.00327 Ωppm^{-1}) (see Fig. 8**c**). The magnitude of change in relative response of sensor 4 is small, and it also has relatively poor sensitivity towards the analytes. Sensor 5 responded to all five analytes, possessing equal sensitivity towards toluene and mesitylene vapours with a maximum sensitivity value of approximately 0.00410 Ωppm^{-1}. Overall, sensor 3 was the best-performing sensor, having a good sensitivity towards the toluene vapour compared to sensors 1, 2, 4,

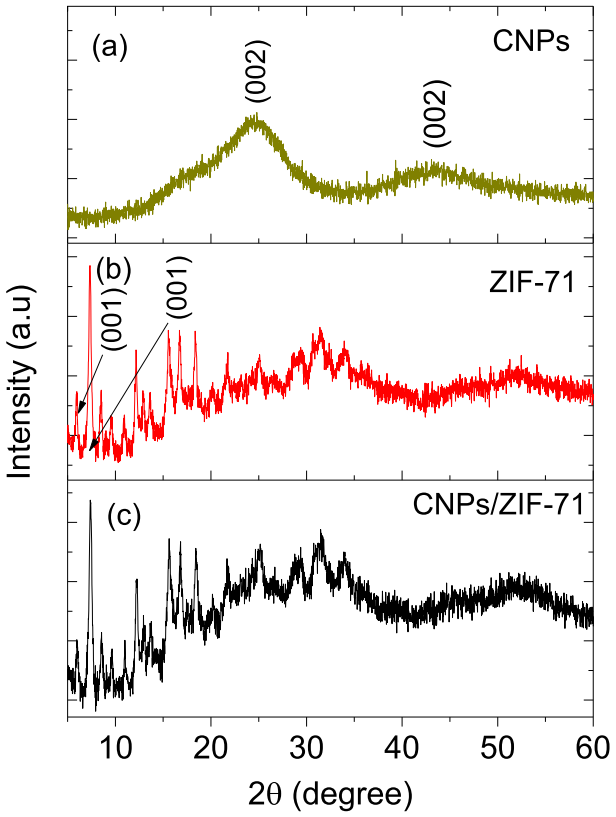

Fig. 4. XRD pattern of (a) CNPs, (b) ZIF-71, and (c) CNPs@ZIF-71.

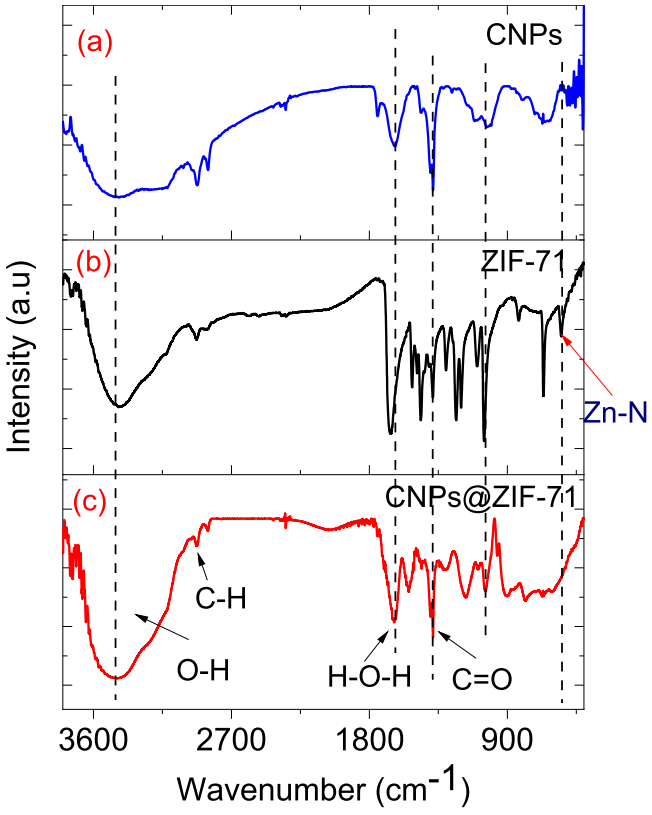

Fig. 5. The FTIR spectra of (a) CNPs, (b) ZIF-71, and (c) CNPs@ZIF-71.

and 5. All the sensors showed a linear increase in relative response as the concentration increased. Sensor 1 has a higher sensitivity towards the analytes than sensor 4. However, sensor 4 showed a low signal-to-noise ratio compared to sensor 1. The relative response in resistance is directly proportional to the vapour concentration (see Fig. 8**b and c**).

The response and recovery time were calculated only for sensor 3 because it is the only sensor that showed higher sensitivity and good selectivity toward the targeted analyte (toluene vapour) over the other tested analytes (refer to histograms in Fig. 8). However, mesitylene vapour is considered as a competitor analyte because the sensor is just 50% less sensitive than the toluene. The response time of toluene vapour of sensor 3 was fast, 42 s; however, the sensor's recovery time after exposure to toluene was slow, 58 s (**see** Table 3). The quicker response time could be due to the higher diffusion rate of toluene vapour towards the active sensing layer, and the other analytes showed slower response times as compared to toluene vapour, which mainly is that the other analytes including acetonitrile, mesitylene, diethyl ether and ethanol vapours have slower diffusion rate around the Sensor [33]. No covalent bond formed between the toluene vapour and the active sensing layer. The pore size of CNPs, ZIF-71, CNPs@ZIF-71 composite with the mass ratio 1:1 obtained from Brunauer-Emmett-Teller (BET) is 336.7 Å, 23.7 Å and 41.7 Å, respectively.

The main factor influencing the analyte gas concentration in the porous structure is the analyte gas's diffusion and surface reaction rate; the latter is also dependent on the pore size and surface diffusion. Even though porous materials primarily use four kinds of diffusion mechanisms, all depend on the pore size of the materials. When the pore size is larger than the mean free path, the bulk Poiseuille flow is dominant [39]; when pores have a diameter ranging from 2 to 50 nm and are long and narrow, the Knudesen diffusion becomes dominant [40]. The third diffusion mechanism becomes dominant when there is a strong potential field between the analyte gas molecules and the pore walls, resulting in the molecules being strongly adsorbed on the pore wall and losing the gaseous property. The adsorbed molecules' diffusion is by vibrating at the adsorption site and slowly moving to the nearby location [41]. When materials with small pore sizes, the translational diffusion mechanism becomes dominant; in this mechanism, the analyte gas molecules require sufficient kinetic energy to break free from one side of the pore wall's surface potential field, and they then diffuse through by leaping from one location to the next [34]. Our prepared material has a pore size of 41.7 Å (CNPs@ZIF-71 composite with a mass ratio 1:1). The kinetic diameter of the analyte molecules are 3.6 Å, 8.6 Å, 6.5 Å, 6.2 Å and 6.5 Å for ethanol, mesitylene, acetonitrile, diethyl ether, and toluene, respectively [35–38,42]. This suggests that the prepared materials' pore size is substantially greater than the kinetic diameter of the analyte molecules. Therefore, there is no hindrance during diffusion through the pores, and the bulk Poiseuille is expected to be the dominant diffusion mechanism. According to our results, the sensor is more sensitive to toluene than the other analytes; it most likely results from surface reactivity of the sensing materials rather than pore size acting as sieving.

3.2.2. Reproducibility and humidity investigations

The repeatability of Sensor 3 was investigated in detecting toluene vapour at room temperature (see Fig. 9**a**). For repeatability studies, Sensor 3 was exposed to 11.5 ppm toluene vapour for five cycles (see Fig. 9**a**). The Sensor's response during the exposure was almost the same, with the maximum response value of 0.25, 0.24, 0.25, 0.25 and 0.24 Ω. The average maximum response was 0.25±0.0005 Ω, indicating that the fabricated sensor was stable during the exposure and read the same value for successive exposure. Thus, Sensor 3 is considered a good sensor since it can respond and regenerate similar results over time. The change in atmospheric moisture or water vapour (commonly known as humidity) affects the gas sensor's performance [43] regarding the response-recovery time, selectivity and the relative response of the gas sensors operating at room temperature [44].

The humidity interferences in the detection of toluene vapour were

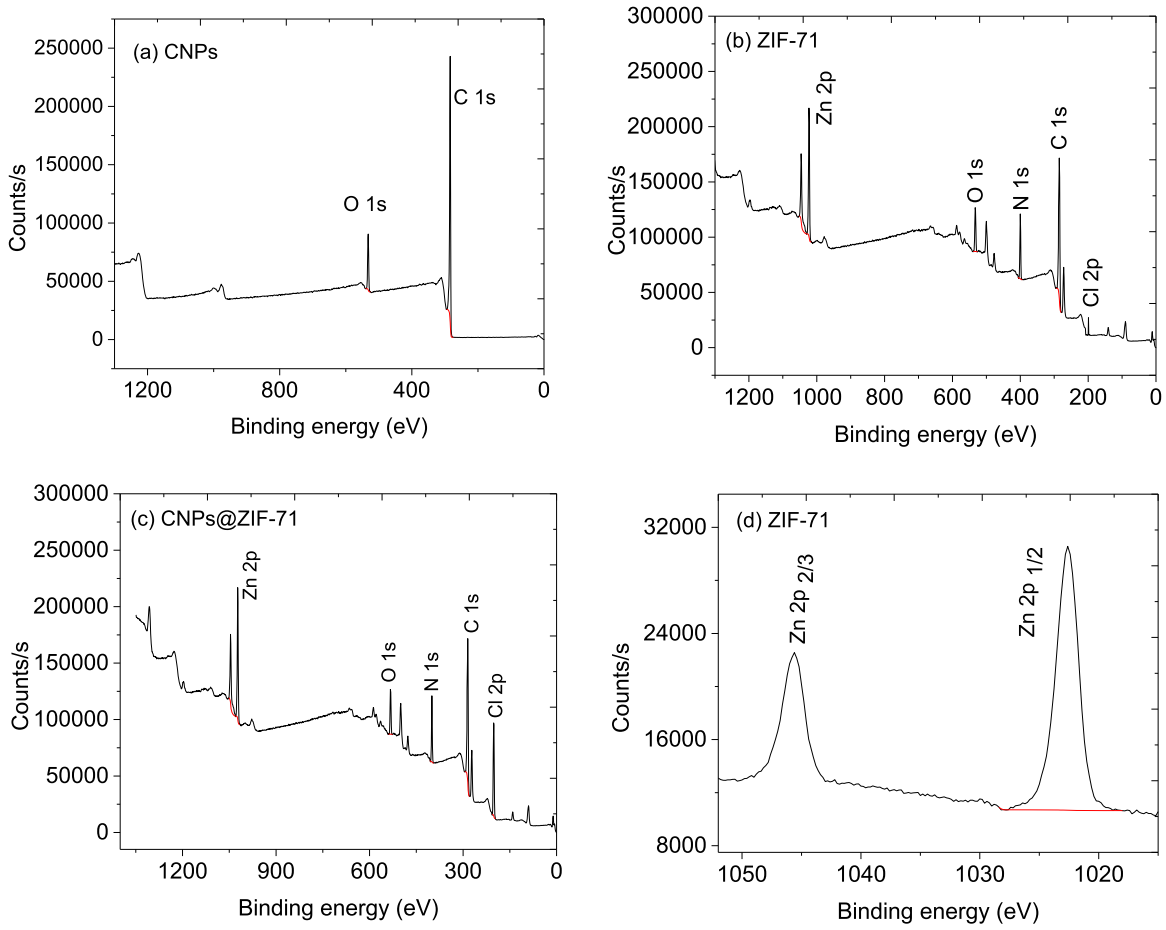

Fig. 6. XPS spectra, (a) CNPs survey, (b) ZIF-71 survey, (c) CNPs@ZIF-71 survey, and (d) Zn 2p scan of ZIF-71.

investigated by injecting a controlled amount of water vapour into the chamber during the detection process. For this experiment, we used 11.5 ppm toluene vapour at variable relative humidity (RH): 33%, 44%, 68%, 80%, and 91% RH and the toluene vapour responses were recorded as 0.20 Ω, 0.23 Ω, 0.25 Ω, 0.27 Ω, and 0.32 Ω, respectively (see Fig. 8**c**). The change in toluene vapour relative response at relative humidities from 33% to 80% RH was only by 0.07 Ω (the difference in maximum response of the vapour), and the average response over the range of humidity was 0.25± 0.040 Ω. It was observed that even at high water molecules content (80% RH), the sensor still responded to toluene vapour with a slight increase in response. However, the response time of toluene is delayed as the humidity increases, which could be that the water vapour molecules condense into liquid water on the surface of CNPs@ZIF-71 composite sensor, and while the recovery time of sensor 3 on toluene vapour increases with an increase in relative humidity (see Fig. 8**d**). The recovery time of the toluene vapour is shortened as the humidity around the sensor increases, mainly because the humidity does not create easy channels for desorbed gases to evacuate the gas chamber. The water molecules are chemisorbed on the sensor's surface, and the water molecules slightly respond to the sensor, which is why the response value of toluene vapour increases as the humidity increases [45]. The slight response could be from the presence of CNPs in sensor 3 (CNPs@ZIF-71, at a mass ratio 1:1) since ZIF-71 is known to be hydrophobic [46].

3.2.3. *Selectivity studies*

Selectivity detection of the targeted toluene vapour was investigated in a mixture vapour (combined all toluene, ethanol, diethyl ether, acetonitrile, and mesitylene vapours in one vessel) on sensor 3 (CNPs@ZIF-71, mass ratio of 1:1) as shown on Fig. 10. The obtained the maximum response curve of the mixture vapour was compared with the maximum response curves of the individual vapours statically detected by sensor 3. The maximum measured relative resistance of the mixture vapour was 0.24 Ω, and targeted toluene vapour was 0.19 Ω, and the poorly responsive analytes, including mesitylene (0.13 Ω), acetonitrile (0.07 Ω), ethanol (0.04 Ω) and diethyl ether (0 Ω). The response curve shape of toluene vapour is almost similar to that of mixture vapour; however, the maximum response value of mixture vapour is a bit higher than that of toluene. The maximum response of toluene vapour should ideally be equal to that of toluene for selectivity measurements; however, the higher response value for the mixture analytes is due to the response interference caused by other vapours. The response time of mixture vapour was higher than for pure toluene was 42 s and for the mixture was 79 s; slowing the response time may be due to competing interference occurring on the surface of the sensing material from other analyte vapour during selective detection of toluene. The delay in response might be that the other vapours (ethanol, acetonitrile, mesitylene, and diethyl ether) occupy some of the active sites of the sensors while detecting the toluene vapour from the mixture vapour.

From reported work, most toluene sensors operate at temperatures of more than 210 °C, as shown in Table 4. However, our sensor is better than the reported work as the sensor operates at room temperature with a fast response-recovery time.

3.2.4. *Sensing mechanism*

CNPs@ZIF-71 Sensor on the detection of toluene vapour gas sensor operating at room temperature uses a gas adsorption-desorption sensing mechanism. Firstly, atmospheric oxygen **gas** molecules adsorb on the surface of the CNPs@ZIF-71 sensor, extracting electrons from the conduction band of the material, and get ionised to generate highly reactive

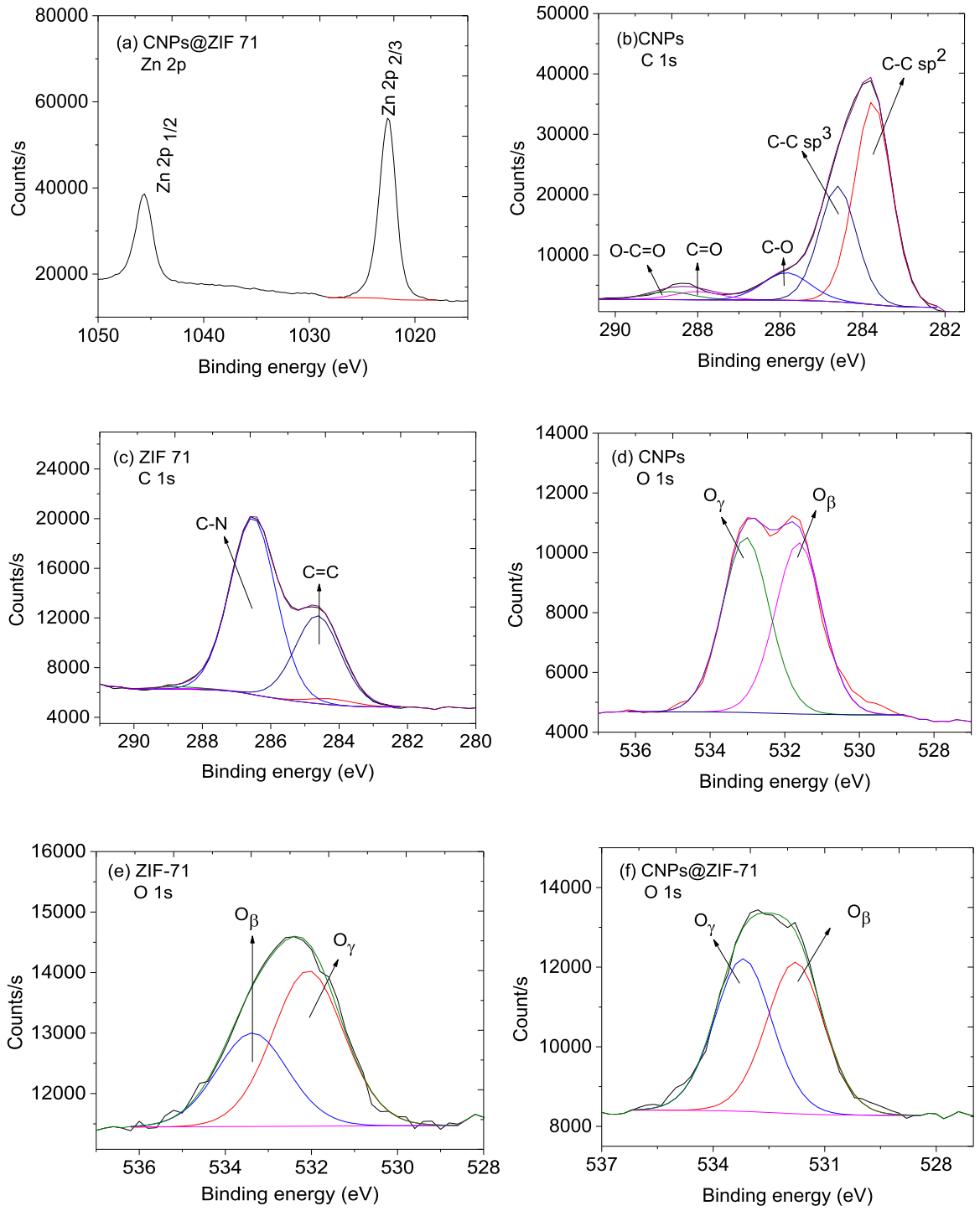

Fig. 7. XPS spectra, (a) Zn 2p of CNPs@ZIF-71, (b) C 1 s scan of CNPs, (c) C 1 s scan of ZIF-71, (d) O 1 s scan of CNPs, (e) O 1 s scan of ZIF-71 and (f) O 1 s scan of CNPs@ZIF-71.

Table 2
The calculated percentage of oxygen species in the materials.

CNPs Peak positioned (eV)	Atomic % of oxygen	ZIF-71 Peak positioned (eV)	Atomic % of oxygen	CNPs@ZIF-71 Peak positioned (eV)	Atomic % of oxygen
O_β →42.7	57.3	O_β →531.7	18.8	O_β →531.7	50
O_γ → 57.3	42.7	O_γ→ 533.1	81.2	O_γ → 533.1	50

oxygen species (O_2^-, O^- and O^{2-}) as represented in Eq. (3)-(5). The oxygen-reactive species, oxides (O^-) and superoxides (O_2^-), are categorised as electrophiles, which attack electron-rich hydrocarbons [52–54]. Furthermore, the O^{2-} are classified as nucleophiles that attack the C—H bonds of the toluene vapour during oxidative dehydrogenation. Consequently, an accumulation of electrons on the surface forms an electron depletion layer, which results in bending the band [55]. The highly reactive oxygen species attack the pie (π) bonds of the toluene vapour [56], which are carbon-to-carbon double bonds (C = C) in the aromatic ring of the toluene. When toluene vapour (C_7H_8) reacts with

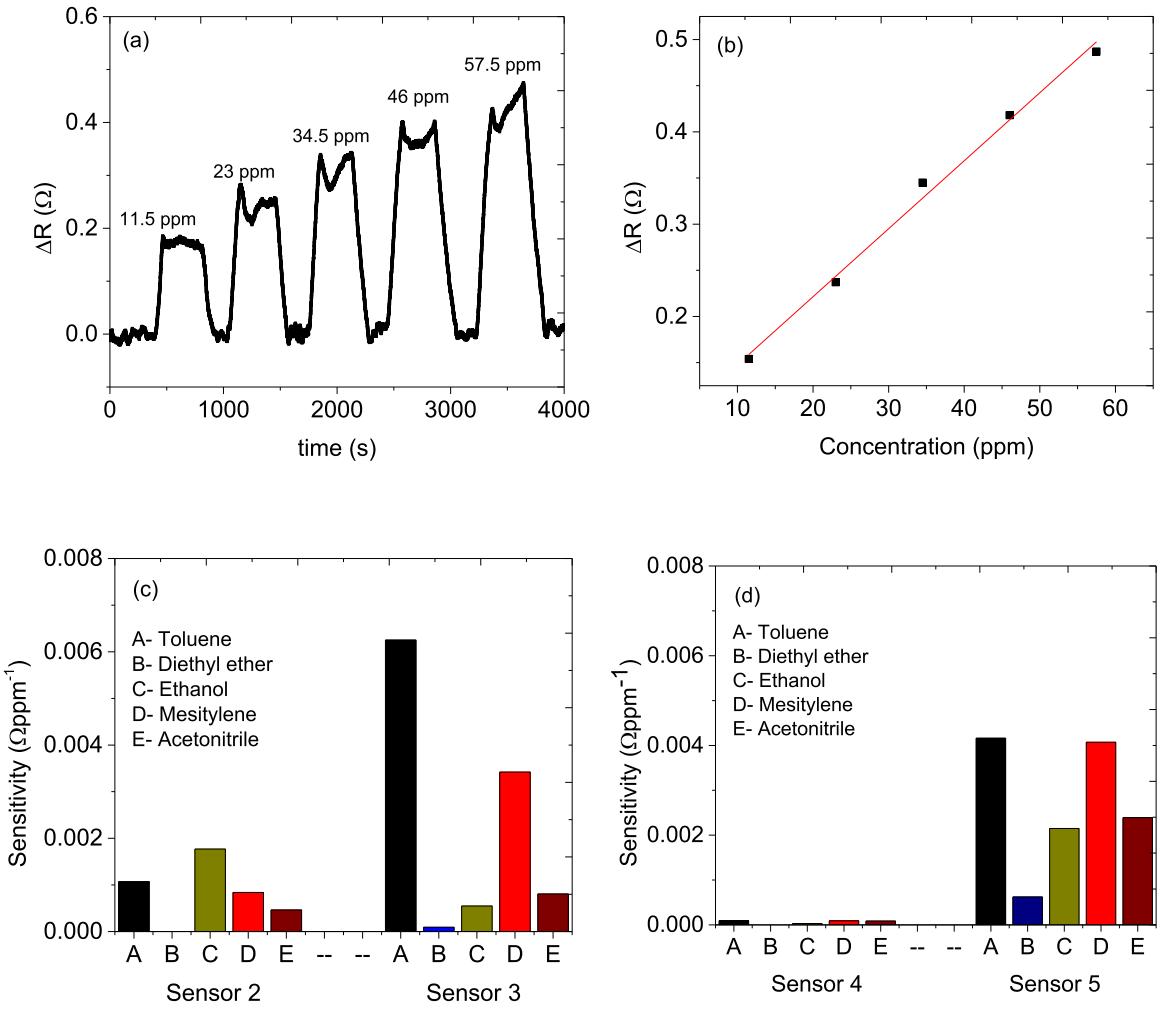

Fig. 8. (a) Relative resistance curve of sensor 3 towards toluene vapour, (b) calibration curve of sensor 3 towards toluene vapour, (c-d) sensitivity bar graph.

Table 3
Comparison of various materials reported of acetone vapour gas sensors.

Analytes	Response time (s)	Recovery (s)	Kinetic diameter (Å)
Ethanol	52	29	3.6 [34]
Mesitylene	96	38	8.6 [35]
Acetonitrile	107	30	6.5 [36]
Diethyl ether	–	–	6.2 [37]
Toluene	42	58	6.5 [38]

(-) not recorded.

the highly reactive oxygen species on the surface of the sensing material, the resistance of the sensing material increases as it loses electrons on the material's surface. As a result, carbon dioxide (CO_2) and water (H_2O) are formed as by-products [23,56]. Atmospheric air containing oxygen is used to flash out the formed CO_2 and H_2O vapour. During the removal of the products formed in the volume chamber, the oxygen molecules chemisorb on the sensor's surface.

The proposed mechanism is toluene vapour reacting with the oxygen-reactive species:

$$O_{2\ (gas)} \rightarrow O_{2\ (ads)} \quad (3)$$

$$\mathbf{O_{2\ (ads)} + e^- \rightarrow O_{2(ads)}^-} \quad (4)$$

$$\mathbf{O_{2(ads)}^- + e^- \rightarrow 2O_{(ads)}^-} \quad (5)$$

$$\mathbf{O_{(ads)}^- + e^- \rightarrow O^{2-}\ (lat)} \quad (6)$$

$$C_7H_{8\ (gas)} + 18O_{(abs)}^- \rightarrow 4H_2O_{\ (gas)} + 7CO_{2\ (gas)} + 18e^- \quad (7)$$

Furthermore, to confirm the sensing mechanism, the *in-situ* FTIR and LCR meter set-up is used to study the sensing mechanism. The ΔR of toluene vapour on Sensor 3 was recorded, as shown in Fig. 11**a,** and the FTIR spectra were collected every minute, as shown in Fig. 11**b**. The CO_2 IR bending mode occurring at 668 cm^{-1} [56] formed during the sensing process, and the C—H stretching (3200- 2900 cm^{-1}) peaks intensities on the aromatic ring were studied. The new CO_2 IR band intensity increased with the time of toluene vapour exposure. The C—H stretching peaks decrease as the time of toluene exposure increases, which gives us insight into the toluene vapour sensing mechanism. Fig. 11**d** presents C—H stretching bands; it is clear that the toluene vapour decomposes into CO_2 and H_2O because the first FTIR spectrum (at $t = 1$ min) has high intensity compared to the last spectrum. The first FTIR spectrum (at $t = 1$ min) recorded shows a little CO_2 intensity as compared to the previously recorded FTIR spectrum (see Fig. 11**c**). With these observations, we have evidence that detecting toluene vapour at room temperature using sensor 3 undergoes deep decomposition.

3.2.5. *Limit of detection (LOD)*

The lowest possible concentration to be detected in gas sensors is important to be known, commonly known as the Limit of Detection (LOD). LOD The calibration curve between the toluene vapour and electrical response gives a correlation coefficient (R^2) of 0.99 and a slope of 0.00637 Ω ppm^{-1}. The LOD = 3 × RMS/slope [38], wherein the RMS

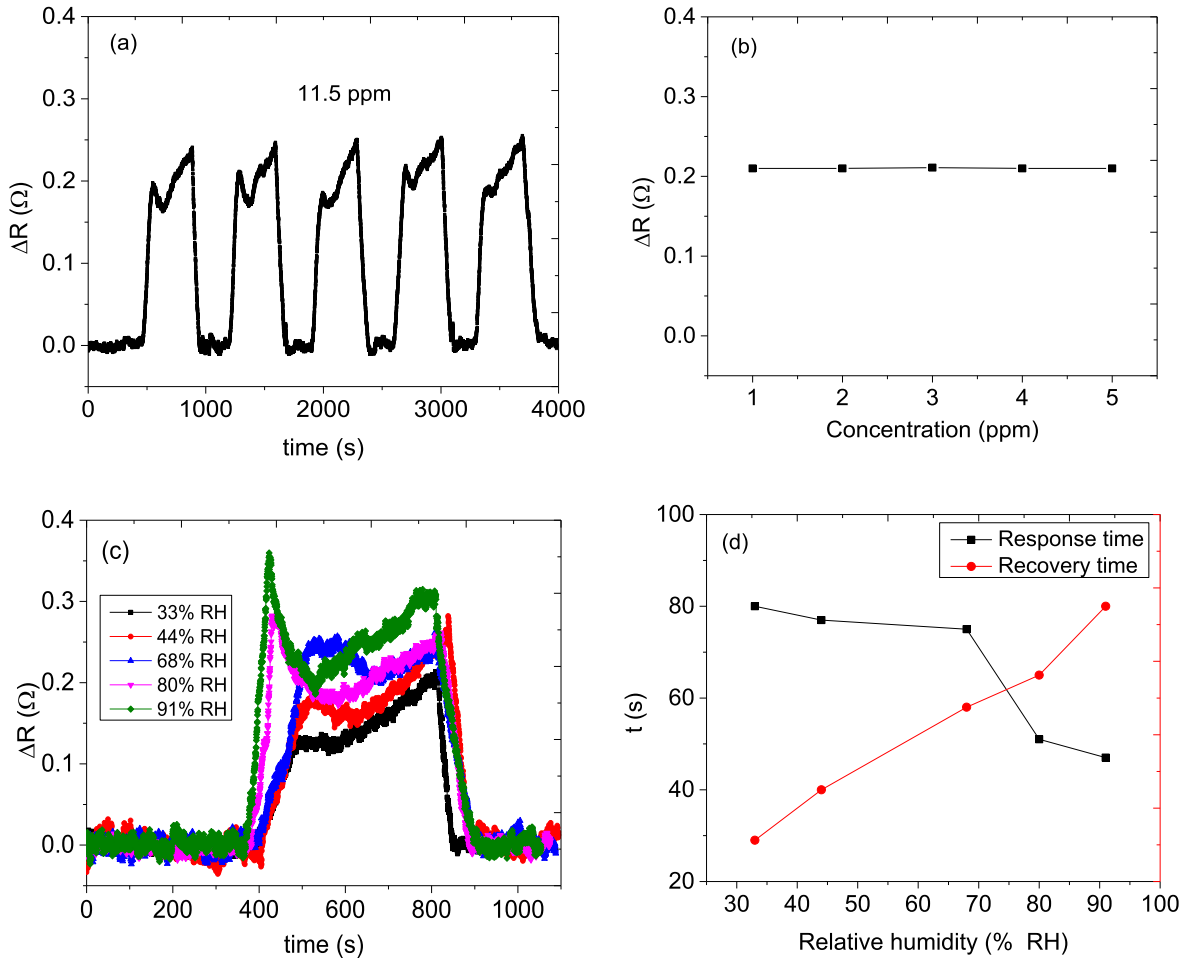

Fig. 9. (a) Repeatability curves of toluene vapour on sensor 3, (b) maximum amplitude of repeatability curves responses, (c) toluene vapour at different humidity conditions, and (d) their relative response-recovery times.

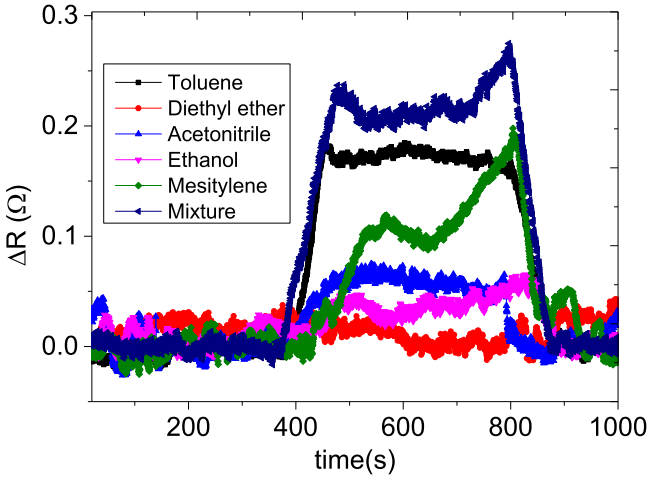

Fig. 10. Static response-recovery curves of the analytes on sensor 3.

is the standard deviation with a value of 0.00011 and the LOD is 518 ppb. CNPs@ZIF-71 (Sensor 3) can detect toluene vapour even at the lowest concentration (ppb).

4. Conclusions

In summary, the successful preparation of CNPs, ZIF-71, and CNPs@ZIF-71 were confirmed using SEM, TEM, PXRD, XPS, and FTIR. CNPs, ZIF-71, and CNPs@ZIF-71 are the materials used to fabricate the sensors for detecting ethanol, toluene, mesitylene, acetonitrile, and diethyl ether vapours. The amount of CNPs within CNPs@ZI-71 composite was varied to investigate the sensors' performance towards the analytes. It was found that CNPs@ZIF-71 with the mass ratio 1:1 (Sensor 3) is highly sensitive to toluene vapour and poorly sensitive towards ethanol, acetonitrile, mesitylene, and diethyl ether. Furthermore, the detection of toluene vapour was done at different humidity conditions, and based on the analysis, there was a slight increase in toluene response as the humidity increased. Sensor 3 is the best and most highly selective sensor on toluene vapour with a LOD of 518 ppb. In situ, FTIR coupled with LCR meter online analysis was done to study the sensing mechanism, and it was found that toluene vapour detection on Sensor 3 undergoes total deep oxidation to form H_2O and CO_2 as by-products.

Table 4
Comparison of various reported toluene vapour gas sensors.

Sensing materials	Toluene (ppm)	Res/rec time (s)	Response (ohms)	Temp (°C)	Ref
Coral like ZnO	3000	–	2.9	25	[47]
Co_3O_4	100	189/1614	11.2	210	[48]
NiO/ZnO	95	70/75	19.1	300	[49]
NiO-SnO_2	50	11.2/4	12	330	[50]
Au-ZnO	100	60/180	8.6	340	[51]
CNPs@ZIF-71	11.5	42/58	0.2	25	**This work**

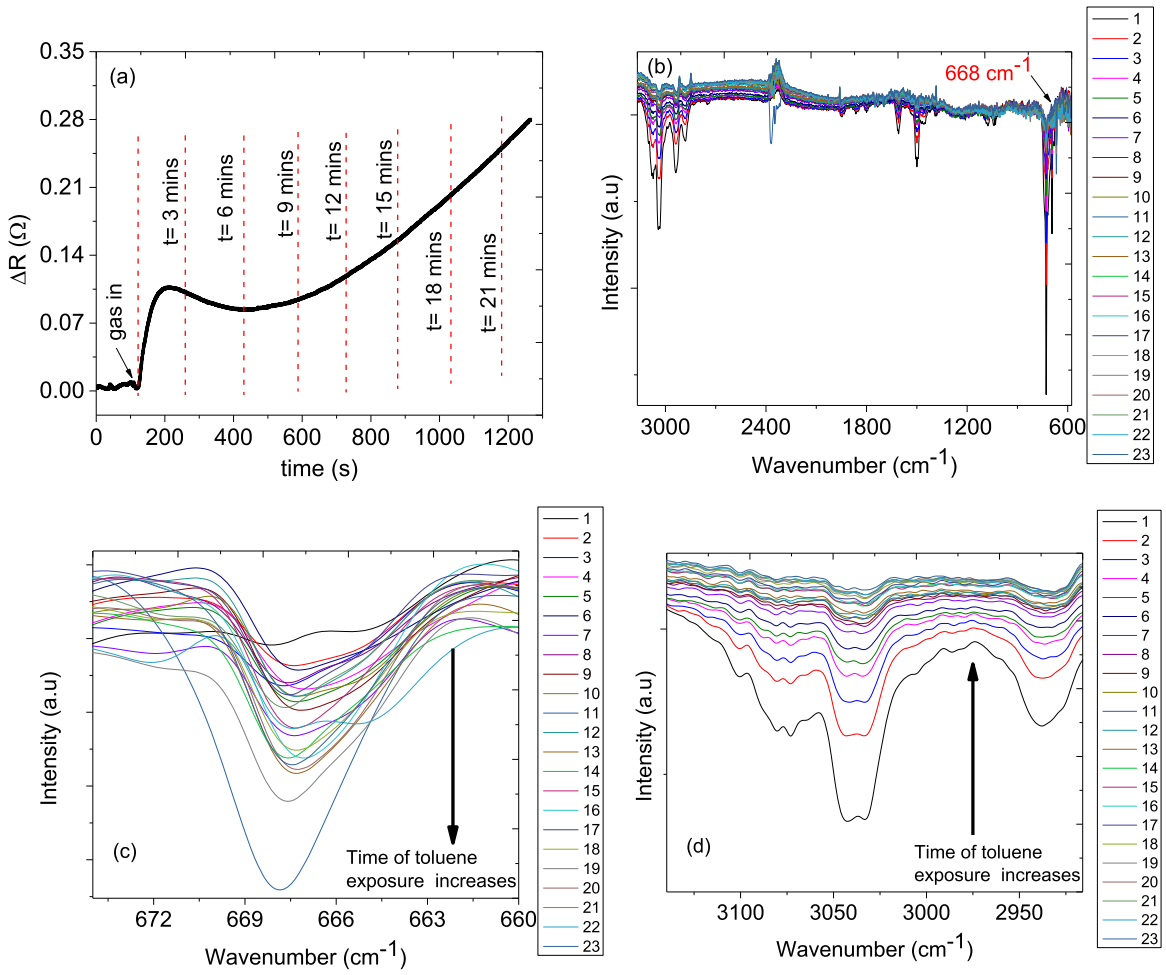

Fig. 11. (a) Response curve of the toluene vapour during in-situ FTIR-LCR meter online analysis, (b) FTIR spectra of toluene vapour during sensing (c) CO_2 IR peak, and (d) C—H stretching of the toluene vapour.

CRediT authorship contribution statement

Lesego Malepe: Writing – original draft, Visualization, Validation, Methodology, Investigation, Formal analysis, Data curation. **Tantoh Derek Ndinteh:** Writing – review & editing, Visualization, Validation, Supervision, Investigation, Formal analysis, Data curation, Conceptualization. **Patrick Ndungu:** Writing – review & editing, Visualization, Validation, Supervision, Investigation, Formal analysis, Data curation, Conceptualization. **Messai Adenew Mamo:** Writing – review & editing, Visualization, Validation, Supervision, Resources, Project administration, Methodology, Investigation, Funding acquisition, Formal analysis, Data curation, Conceptualization.

Declaration of competing interest

There are no conflicts to declare. The manuscript was written with contributions from all authors.

Data availability

Data will be made available on request.

Acknowledgements

Lesego Malepe thanks the University of Johannesburg for financial assistance. All authors acknowledge the University of Johannesburg for financial assistance.

Supplementary materials

Supplementary material associated with this article can be found, in the online version, at doi:10.1016/j.materresbull.2024.113076.

References

[1] W. HaiLin, N. Lie, L. Jing, W. YuFei, W. Gang, W. JunHui, H.Z. Ping, Characterisation and assessment of volatile organic compounds (VOCs) emissions from typical industries, Chin. Sci. Bull. 80 (2013) 724–730.
[2] D. Zhang, C. Jiang, X. Zhou, Fabrication of Pd-decorated TiO_2/MoS_2 ternary nanocomposite for enhanced benzene gas sensing performance at room temperature, Talanta 182 (2018) 324–332.
[3] X. Liang, X. Sun, Q. Lu, L. Ren, M. Liu, Y. Su, S. Wang, H. Lu, B. Gao, W. Zhao, VOC emission inventory of architectural coatings and adhesives for new buildings in China based on investigated and measured data, Atmos. Environ. 245 (2021) 118014.
[4] Z. Cai, J. Park, S. Park, Porous In_2O_3–ZnO nanofiber-based sensor for ultrasensitive room-temperature detection of toluene gas under UV illumination, J. Mater. Res. Technol, 24 (2023) 2482–2499.
[5] O. Jimenez-Garza, L. Guo, H.M. Byun, M. Carrieri, G.B. Bartolucci, B.S. Barron-Vivanco, A. Baccarelli, Aberrant promoter methylation in genes related to hematopoietic malignancy in workers exposed to a VOC mixture, Toxicol. Appl. Pharmacol. 339 (2018) 65–72.
[6] H. Ji, Y. Liu, R. Zhang, Z. Yuan, F. Meng, Detection and recognition of toluene and butanone in mixture based on SnO_2 sensor via dynamic transient and steady-state response analysis in jump heating voltage mode, Sens. Actuat. B. 376 (2023) 132969.
[7] H.L. Li, H.Y. Zhan, S.Y. Fu, Rapid determination of methanol in black liquors by full evaporation headspace gas chromatography, J. Chromatogr. A. 1175 (2007) 133–136.

[8] J.W. Lin, S.Y. Shaw, The potential of CO_2 laser photoacoustic spectrometry for detection of methanol in alcoholic beverage, Sens. Actuat. B. 94 (2009) 535–544.
[9] K. Wrobel, D.M. Rodríguez, F.J.A. Aguilar, Determination of methanol in o,o-dimethyl dithiophosphoric acid (DMDTPA) of technical grade by UV/vis spectrophotometry and by HPLC, Talanta 66 (2005) 125–129.
[10] C. Wang, L. Yin, L. Zhang, D. Xiang, R. Gao, Metal oxide gas sensors: sensitivity and influencing factors, Sensors 10 (2010) 2088–2106.
[11] M. Lesego, D.T. Ndinteh, P. Ndungu, M.A. Messai, Zeolitic imidazolate framework as humidity-resistant solid state-chemiresistive gas sensors: a review, Heliyon 9 (2023) 22329.
[12] M. Subramanian, V.V. Dhayabaran, M. Shanmugavadivel, Room temperature fiber optic gas sensor technology based on nanocrystalline $Ba_3(VO_4)_2$: design, spectral and surface science, Mater. Res. Bull. 119 (2019) 110560.
[13] A.P. Lee, B.J. Reedy, Temperature modulation in semiconductor gas sensing, Sens. Actuat. B. 60 (1999) 35–42.
[14] S. Fan, W. Tang, Synthesis, characterisation and mechanism of electrospun carbon nanofibers decorated with ZnO nanoparticles for flexible ammonia gas sensors at room temperature, Sens. Actuat. B. 362 (2022) 131789.
[15] L. Malepe, D.T. Ndinteh, M.A. Mamo, The effect of measurement parameters on the performance of the sensors in the detection of organic compound vapours, Chem. Phys. Impact 4 (2022) 100068.
[16] S. Varghese, S. Varghese, S. Swaminathan, K. Singh, V. Mittal, Two-dimensional materials for sensing: graphene and beyond, Electronics. 4 (2015) 651–687.
[17] S. Mun, Y. Chen, J. Kim, Cellulose-titanium dioxide-multiwalled carbon nanotube hybrid nanocomposite and its ammonia gas sensing properties at room temperature, Sens. Actuat. B. 56 (2012) 87–94.
[18] S. Kwon, H. Choi, S. Lee, G. Lee, Y. Kim, W. Choi, H. Kang, Room temperature gas sensor application of carbon nanowalls using electrical resistance change by surface adsorption of toxic gases, Mater. Res. Bull. 141 (2021) 111377.
[19] T. Zhou, Y. Sang, Y. Sun, C. Wu, X. Wang, X. Tang, T. Zhang, H. Wang, C. Xie, D. Zeng, Gas adsorption at metal sites for enhancing gas sensing performance of ZnO@ZIF-71 nanorod arrays, Langmuir 35 (2019) 3248–3255.
[20] Y. Zhou, T. Zhou, Y. Zhang, L. Tang, Q. Guo, M. Wang, Synthesis of core-shell flower-like WO_3@ZIF-71 with enhanced response and selectivity to H_2S gas, Solid State Ionics 350 (2020) 115278.
[21] N. Garg, M. Kumar, N. Kumari, A. Deep, A.L. Sharma, Chemoresistive room-temperature sensing of ammonia using zeolite imidazole framework and reduced graphene oxide (ZIF-67/RGO) composite, ACS Omega 5 (2020) 27492–27501.
[22] M. Tu, C. Wiktor, C. Rosler, R.A. Fischer, Rapid room temperature syntheses of zeolitic-imidazolate framework (ZIF) nanocrystals, Chem. Commun. 50 (2014) 13258–13260.
[23] L. Malepe, P. Ndungu, D. Ndinteh, M.A. Mamo, Nickel oxide-carbon soot-cellulose acetate nanocomposite for the detection of mesitylene vapour: investigating the sensing mechanism using an LCR meter coupled to an FTIR spectrometer, Nanomaterials 12 (2022) 727.
[24] L. Malepe, P. Ndungu, T.D. Ndinteh, M.A. Messai, An in-situ FTIR-LCR meter technique to study the sensing mechanism of MnO_2@ZIF-8/CNPs and a direct relationship between the sensitivity of the sensors and the rate of surface reaction, Result. Phys. 52 (2023) 106864.
[25] Y. Wang, Q. Shi, H. Xua, J. Dong, The synthesis and tribological properties of small- and large-sized crystals of zeolitic imidazolate framework-71, RSC Adv. 6 (2016) 18052–18059.
[26] X. Dong, Y.S. Lin, Synthesis of an organophilic ZIF-71 membrane for pervaporationsolvent separation, Chem. Commun. 49 (2013) 1196–1198.
[27] R. Banerjee, A. Phan, B. Wang, C. Knobler, H. Furukawa, M. O'Keeffe, O.M. Yaghi, High-throughput synthesis of zeolitic imidazolate frameworks and application to CO_2 capture, Science 319 (2008) 939.
[28] N. Tiempos-Flores, E. Hernández-Fernández, A. Rico-Barragan, J.R. Álvarez, I. Juárez-Ramírez, M.A. Garza-Navarro, J. Rodríguez-Hernández, A. Fonseca-García, D.J. Michaelis, N.E. Davila-Guzman, Enhanced hydrophobicity of modified ZIF-71 metal-organic framework for biofuel purification, Polyhedron 217 (2022) 115736.
[29] S. Japip, H. Wang, Y. Xiao, T.S. Chung, Highly permeable zeolitic imidazolate framework (ZIF)-71 nanoparticles enhanced polyimide membranes for gas separation, J. Membr. Sci. 467 (2014) 162–174.
[30] S. Feng, X. Jia, J. Yang, Y. Li, S. Wang, H. Song, One-pot synthesis of core–shell ZIF-8@ZnO porous nanospheres with improved ethanol gas sensing, J. Mater. Sci.: Mater. Electron. 31 (2020) 22534–22545.
[31] C.K. Gaddam, R.L. Vander Wal, Physical and chemical characterisation of SIDI engine particulates, Combust. Flame 160 (2013) 2517–2528.
[32] F. Chenyang, S. Chonglin, L. Gang, W. Jiangjun, Z. Xuyang, Q. Yuehan, L. Ye, Impact of post-injection strategy on the physicochemical properties and reactivity of diesel in-cylinder soot, Proc. Combust. Inst. 37 (2019) 4821–4829.
[33] J.W. Gardner, A Non-Linear diffusion-reaction model of electrical conduction in semiconductor gas sensors, Sens. Actuat. B. 1 (1990) 166.
[34] T. Yoshioka, T. Tsuru, M. Asaeda, Molecular dynamics studies on gas permeation properties through microporous silica membranes, Sep. Purif. Tech. 25 (2001) 441–449.
[35] S.F. Zaman, K.F. Loughlin, S.A. Al Khattaf, Kinetics of desorption of 1,3-diisopropylbenzene and 1,3,5-triisopropylbenzene. 2. diffusion in FCC catalyst particles by zero length column method, Ind. Eng. Chem. Res. 16 (2015) 4572–4580.
[36] S.C. Lee, S.Y. Kim, W.S. Lee, S.Y. Yung, B.W. Hwang, D. Ragupathy, D.D. Lee, S. Y. Lee, J.C. Kim, Effects of textural properties on the response of a SnO_2-based gas sensor for the detection of chemical warfare agents, Sensors 11 (2011) 6893–6904.
[37] T. Omojola, I.P. Silverwood, A.J. O'Malley, Molecular behaviour of methanol and dimethyl ether in H-ZSM-5 catalysts as a function of Si/Al ratio: a quasielastic neutron scattering study, Catal. Sci. Technol. 10 (2020) 4305–4320.
[38] M.A. Hernández, L. Corona, A.I. González, F. Rojas, V.H. Lara, F. Silva, Quantitative study of the adsorption of aromatic hydrocarbons (benzene, toluene, and p-xylene) on dealuminated clinoptilolites, Ind. Eng. Chem. Res. 9 (2005) 2908–2916.
[39] S.T. Oyama, H. Aono, A. Takagaki, T. Sugawara, R. Kikuchi, Synthesis of silica membranes by chemical vapor deposition using a dimethyldimethoxysilane precursor, Membranes (Basel) 10 (2020) 50.
[40] K. Malek, M. Coppens, Knudsen self- and Fickian diffusion in rough nanoporous media, J. Chem. Phys. 119 (2003) 2801–2811.
[41] D.N. Jaguste, S.K. Bhatia, Combined surface and viscous flow of condensable vapor in porous media, Chem. Eng. Sci. 50 (1995) 167.
[42] Y. Tang, D. Dubbeldam, S. Tanase, Water–ethanol and methanol–ethanol separations using in situ confined polymer chains in a metal–organic framework, ACS Appl. Mater. Interfaces. 44 (2019) 41383–41393.
[43] J. Wang, P. Yang, X. Wei, High-performance, room-temperature, and no-humidity-impact ammonia sensor based on heterogeneous nickel oxide and zinc oxide nanocrystals, ACS Appl. Mater. Interface. 7 (2015) 3816–3824.
[44] W. Yan, M.A. Worsley, T. Pham, A. Zettl, C. Carraro, R. Maboudian, Effects of ambient humidity and temperature on the NO_2 sensing characteristics of WS_2/graphene aerogel, Appl. Surface Sci. 450 (2018) 372–379.
[45] T.A. Blank, L.P. Eksperiandova, K.N. Belikov, Recent trends of ceramic humidity sensors development: a review, Sens. Actuat. B. 228 (2016) 416–442.
[46] N. Tiempos-Flores, E. Hernández-Fernández, A. Rico-Barragan, J.R. Álvarez, I. Juárez-Ramírez, M.A. Garza-Navarro, J. Rodríguez-Hernández, A. Fonseca-García, D.J. Michaelis, N.E. Davila-Guzman, Enhanced hydrophobicity of modified ZIF-71 metal-organic framework for biofuel purification, Polyhedron 217 (2022) 115736.
[47] K. Arshak, I. Gaidan, and NiO/Fe_2O_3 polymer thick films as room temperature gas sensors, Thin Solid Film. 495 (2006) 286–291.
[48] L. Wang, S.Y. Song, B. Hong, J.C. Xu, Y.B. Han, H.X. Jin, D.F. Jin, J. Li, Y.T. Yang, X.L. Peng, H.L. Ge, X.Q. Wang, Highly improved toluene gas-sensing performance of mesoporous Co_3O_4 nanowires and physical mechanism, Mater. Res. Bull. 140 (2021) 111329.
[49] S. Dey, S. Nag, S. Santra, S.K. Ray, P.K. Guha, Voltage-controlled NiO/ZnO p-n heterojunction diode: a new approach towards selective VOC sensing, Microsyst. Nanoeng. 6 (2020) 9.
[50] L. Liu, Y. Zhang, G. Wang, S. Li, L. Wang, Y. Han, X. Jiang, A. Wei, High toluene sensing properties of NiO–SnO_2 composite nanofiber sensors operating at 330 °C, Senso. Actuat. B 160 (2011) 448–454.
[51] L. Wang, S. Wang, M. Xu, X. Hu, H. Zhang, Y. Wang, W. Huang, A Au-functionalized ZnO nanowire gas sensor for detection of benzene and toluene, Phys. Chem. Chem. Phys. 15 (2013) 17179–17186.
[52] Z. Zhang, Z. Wen, Z. Ye, L. Zhu, Gas sensors based on ultrathin porous Co_3O_4 nanosheets to detect acetone at low temperature, RSC Adv. 5 (2015) 59976–59982.
[53] O. Okechukwu, V. Mavumengwana, I.A. Hümmelgen, M.A. Messai, Concomitant in situ FTIR and impedance measurements to address the 2-methylcyclopentanone vapor-sensing mechanism in MnO_2–polymer nanocomposites, ACS Omega 4 (2019) 8324–8333.
[54] Q. Jia, H. Ji, Y. Zhang, Y. Chen, X. Sun, Z. Jin, Rapid and selective detection of acetone using hierarchical ZnO gas sensor for hazardous odor markers application, J. Hazard. Mater. 276 (2014) 262–270.
[55] S.P.S. David, S. Veeralakshmi, J. Sandhya, S. Nehru, S. Kalaiselvam, Room temperature operatable high sensitive toluene gas sensor using chemiresistive Ag/Bi_2O_3 nanocomposite, Sens. Actuat. B. 320 (2020) 128410.
[56] V.O. Okechukwu, V. Mavumengwana, M.A. Messai, A direct relationship between the sensitivity of the sensors and the intensity of IR CO_2 peak in in situ FTIR-LCR meter chemi-impedance SnO_2–carbon nanoparticles polymer-based sensors in the detection of organic compounds vapor, AIP Adv. 11 (2021) 105203.